Multiscale investigations on Interfacial Behavior of nanoscale systems

Yeau-Ren Jeng, Professor
Department of Mechanical Engineering,
National Chung Cheng University,
Ming-Hsiung, Chia-Yi 621,
TAIWAN

Report Documentation Page

1. REPORT DATE **19 MAR 2010**	2. REPORT TYPE **Final**	3. DATES COVERED **01-07-2008 to 01-10-2009**	
4. TITLE AND SUBTITLE **Multi-Scale Investigation on Interfacial Behavior of Nano-Systems**		5a. CONTRACT NUMBER **FA48690814085**	
		5b. GRANT NUMBER	
		5c. PROGRAM ELEMENT NUMBER	
6. AUTHOR(S) **Yeau-Ren Jeng**		5d. PROJECT NUMBER	
		5e. TASK NUMBER	
		5f. WORK UNIT NUMBER	
7. PERFORMING ORGANIZATION NAME(S) AND ADDRESS(ES) **National Chung Cheng University,168 University Road, Ming-Hsiung,Chia-Yi ,Taiwan,TW,621**		8. PERFORMING ORGANIZATION REPORT NUMBER **N/A**	
9. SPONSORING/MONITORING AGENCY NAME(S) AND ADDRESS(ES) **Asian Office of Aerospace Research & Development, \(AOARD), Unit 45002, APO, AP, 96338-5002**		10. SPONSOR/MONITOR'S ACRONYM(S) **AOARD**	
		11. SPONSOR/MONITOR'S REPORT NUMBER(S) **AOARD-084085**	
12. DISTRIBUTION/AVAILABILITY STATEMENT **Approved for public release; distribution unlimited**			
13. SUPPLEMENTARY NOTES			

14. ABSTRACT

This research is a concerted team effort to investigate the multiscale behavior of materials systems made of nano-materials or nano/bulk-materials. The fundamental understanding of multiscale behavior is the key to the utilization of nano-materials and to the design of material systems contained nano-materials. The research program represents a synergistic effort to investigate different aspects of multiscale phenomena using the computational approaches by a team composed of researchers from AFRL-ML, NCCU of Taiwan and US universities. Mixed atomistic and continuum methods offer the possibility of carrying out simulations of material properties at both larger length scales and longer times than direct atomistic calculations. The proposed innovative algorithm links atomistic and continuum models through the device of the finite element method which permits a reduction of the full set of atomistic degrees of freedom. This research gives a full description of the proposed innovative algorithm with special reference to the ways in which the method may be used to model crystals with more than a single grain. In this project, we have developed the innovative algorithms in the area of nanomechanics. These approaches were used to studies the nanoindentation size effect, mechanical properties of nanotubes, the effect of adsorbed layers on the mechanical properties of thin films, and the asperity contact at nano-scale interfaces.

15. SUBJECT TERMS
Modelling & Simulation, multiscale

16. SECURITY CLASSIFICATION OF:			17. LIMITATION OF ABSTRACT	18. NUMBER OF PAGES	19a. NAME OF RESPONSIBLE PERSON
a. REPORT **unclassified**	b. ABSTRACT **unclassified**	c. THIS PAGE **unclassified**	**Same as Report (SAR)**	**55**	

Abstract

This research is a concerted team effort to investigate the multiscale behavior of materials systems made of nano-materials or nano/bulk-materials. The fundamental understanding of multiscale behavior is the key to the utilization of nano-materials and to the design of material systems contained nano-materials. The research program represents a synergistic effort to investigate different aspects of multiscale phenomena using the computational approaches by a team composed of researchers from AFRL-ML, NCCU of Taiwan and US universities.

Mixed atomistic and continuum methods offer the possibility of carrying out simulations of material properties at both larger length scales and longer times than direct atomistic calculations. The proposed innovative algorithm links atomistic and continuum models through the device of the finite element method which permits a reduction of the full set of atomistic degrees of freedom. This research gives a full description of the proposed innovative algorithm with special reference to the ways in which the method may be used to model crystals with more than a single grain.

In this project, we have developed the innovative algorithms in the area of nanomechanics. These approaches were used to studies the nanoindentation size effect, mechanical properties of nanotubes, the effect of adsorbed layers on the mechanical properties of thin films, and the asperity contact at nano-scale interfaces.

Introduction

Nanotechnology holds great promise to create novel materials that would have profound impact on the way people live their lives. A nano-system is usually made of nano-materials or nano/bulk-materials and thereby multi-scale in nature. A fundamental understanding of multi-scale behavior is the key to the utilization of nano-materials and to the design and fabrication of nano systems. Moreover, the nanotechnology enabled multi-scale characterization of mechanical properties and interfacial phenomena will provide physical insight that was not available before and thereby lead to a multi-functional, robust, and durable nano-system. The proposed research will developed multi-scale approaches that combine the models of different scales, effectively concentrating the computational power where it is needed the most to balance accuracy and efficiency. These approaches will then be used for the investigation of mechanical properties and interfacial phenomena of various nano-materials ranging from thin film, nanotubes to biomaterials. The proposed program represents a concerted team effort to investigate different aspects of multi-scale phenomena by a team composed of researchers from NCCU of Taiwan led by Professor Yeau-Ren Jeng, efforts of AFRL/MLBP led by Dr. John Maguire, and Professor Tay Tang Earn of National University of Singapore. This team represents the core group working on multi-scale phenomena for AFOSR. This team has organized an international workshop on *Challenges in Computer Simulation: Bridging the Time and Length Scales* to be held in Singapore in July 2007. The purpose of this workshop is to provide an international forum at which world leaders present and discuss critically the most recent advances in atomistic and meso-scale modeling and how to bridge the time and distance scale gap and identify and prioritize a small number of "Grand Challenge" problems. We are also discussing with

3

Professor Rodney Ruoff of Northwestern University regarding the measurement of mechanical properties of nanotubes using his novel test rig.

The behavior of solid surfaces in close proximity or in contact is pivotal in the utilization of nano-materials and the design of material systems contained nano-materials. Furthermore knowledge of the mechanical properties of nano-materials is essential in the quantification of interfacial behavior and the development of nano-scale devices. Hence the proposed integrated project is aimed to investigate the interfacial behavior and mechanical properties of nano-materials. The study on interfacial behavior will include adhesion and tribology. The investigation on mechanical properties covers two widely used nanostructures, thin films and nanotubes. They have been proposed as the functional units for the construction of the future molecular-scale machines, and highly complex nanoelectromechanical systems (NEMS). Thin films are such important basic elements for advanced functional materials and devices that understanding their mechanical properties becomes more and more important. Single-walled carbon nanotubes (SWCNTs) were first discovered in 1993 [1, 2]. Since then, carbon nanotubes have been the subject of growing attention within the scientific community as a result of their unique structural, physical, electrical and mechanical properties, and their potential for use in a variety of practical applications [3–6]. More recent investigations of non-carbon nanotubes composed of a significant variety of chemical compositions have reported that these materials possess very high stiffness and strength characteristics. These nanotubes include BN composite nanotubes [9–12], Mo and W chalcogenide tubes [13–16], NiCl cage structures [17], GaSe [18] and GaN [19–24] nanotubes. The remarkable mechanical properties and nanometer-scale sizes render them promising candidates for use as nanometer-scale wires and properly joined individual nanotubes could be the building blocks of various electronic devices. It is clear that interfacial behavior

4

and mechanical properties derived from bulk material are most likely erroneous for nano-scale materials. Their properties may vary locally over nanometer dimensions. Therefore, the determination of *in situ* mechanical behavior for nano-scale materials plays a crucial role for the development of nanoscience and a better understanding of nano-scale property can lead to unique nanostructures and innovative nanosystems for a wide range of applications including aerospace.

Nanoindentation is a well-known means of determining mechanical properties through the analysis of the load-depth curve obtained from the indentation of nano-scale dimension [25-28]. However, the analysis of the load-depth curve based on Hertz contact theory breaks down when the indentation depth falls in the nanometer regime. Hence, computer simulations of nanoindentation are of increasing interest. Perez *et al.* [29] employed total-energy pseudo-potential calculations to study the plastic behavior which occurs during nanoindentation, and concluded that these plastic deformations are activated by charge delocalizations. Zimmerman *et al.* [30] conducted atomistic simulations to clarify the surface step effects on nanoindentation. Their results indicated that the yielding load decreases when indentation takes place in the vicinity of a surface step. Fuente *et al.* [31] studied nanoindentation using scanning tunneling microscopy and atomistic simulations, in which the dislocation loops observed experimentally were successfully reproduced. J. Knap *et al.* [32] addressed the effects of the indenter radius size on the nanoindentation of Au (001), and demonstrated that the indenter force is an unreliable indicator of the onset of dislocation for indenter sizes in the experimental range. In addition, Minot *et al.* [33] found that the mechanical and electrical properties of the nanotubes were affected by contact deformation via nanoindentation techniques. Walters *et al.* [34] and Decossas *et al.* [35] measured the elastic strain and the elastic moduli, respectively, of SWCNT ropes using an AFM probe. Thereby, nanoindentation has emerged as a powerful

technique for determining the surfaces physics in condensed matter and the mechanical properties of nanomaterials in the nanometer regime. In practice, material surfaces are invariably coated with a very thin layer of material known as an "adsorbed layer" [36-38]. Typically, this layer may be made up of a thin coating of impurities or may take the form of a few angstroms of hydrocarbons and water adsorbed on the surface following its exposure to air. In evaluating the mechanical properties of a material using nanoindentation in the ultra-low depth regime, the effects of these adsorbed layers must be taken into account. He *et al.* [37] explored the effect of adsorbed layers on the static friction (Fs) properties of a contact pair and argued that two bodies in sliding contact become locked together to form a local energy minimum and therefore require the Fs to separate them. According to their results, the presence of an adsorbed layer on one or both of the contact surfaces reduced the strength of the bonding force between them and therefore had a direct impact on the static friction properties of the contact. Whereas, developing insights into the influence of adsorbed layers on the mechanical and tribological properties of a material under nanoindentation is essential to ensure a reliable interpretation of the nanoindentation results.

Over the recent years, Molecular Dynamic (MD) has proved to be a powerful tool for the study of nano-materials, concerned with the nano-scale mechanics and thermodynamics. Due to the large number of atoms and the large time scales involved in the structural and thermal properties of simulated system, the use of accurate quantum techniques in the description of these systems becomes impractical even if not completely unfeasible. The conventional finite element method is not suitable since they cannot describe the interactions between atoms. Therefore, the more reliable and computational efficient MD methods have been employed to mimic the atom–atom interactions. Since the primary concern of nano-interface is atom to atom

interactions, MD is a suitable computational tool. However, MD simulation is still very time-consuming due to its associated time resolutions of a pico-second or less. Therefore, for phenomena where atom fluctuations are not important such as contact behavior or nanoindentation, the proposed research will adopt an alternative approach based on the fact that in condensed systems, atoms or molecules always oscillate around the minimum-energy positions. The computation in this way is quasi-static, thereby greatly reducing the computation time. We also utilized an approach which resembles FEM (Finite Element Method) methodology to locate the minimum-energy positions effectively.

We employed the modified FEM approach to study the contact behavior in the interface of two solid surfaces and simulate elastic-plastic deformations in a copper substrate during a complete nanoindentation cycle. The indentation size effect and void effect were explored and discussed. We also utilized the atomic FEM approach to investigate the contact behavior at nano-scale interfaces.

In the mean time, we used a series of experimental nanoindentation tests and molecular dynamics simulations to investigate buckling instabilities of carbon nanotube probes. Developing an improved understanding of mechanical properties and structural deformations of such nanotube probes is beneficial in evaluating their imaging capabilities and limitations.

Approach

I. Nano-mechanics Computational Algorithm

In the proposed approach, atoms are regarded as nodes, and their potentials are considered to be elements. It is assumed that atom, i, is located at position (x_i, y_i, z_i) with displacements u_i, v_i and w_i in the x- , y- and z-directions, respectively. By

defining the nodal displacement vector for the i atom as $\{u\}_i$ and the corresponding external nodal force vector as $\{F\}_i = (f_i, g_i, h_i)^T$, the total potential energy for atom, i, can be expressed as:

$$E_i = \frac{1}{2}\sum_{j \neq i}\phi(r_{ij}) + F(\sum_{j \neq i}f(r_{ij})) - \{u\}_i^T\{F\}_i \tag{5}$$

where the atomic distance r_{ij} is given by:

$$r_{ij} = \left\{(x_i + u_i - x_j)^2 + (y_i + v_i - y_j)^2 + (z_i + w_i - z_j)^2\right\}^{1/2} \tag{6}$$

The differential of the atomic distance with respect to $\{u\}_i$ can be expressed as:

$$dr_{ij} = \frac{1}{r_{ij}}\left[x_i + u_i - x_j, \; y_i + v_i - y_j, z_i + w_i - z_j\right]d\{u\}_i$$

$$= [B]d\{u\}_i \tag{7}$$

The principle of minimum work enforces the minimization of the total energy of the whole system ($E_{total} = \sum_i E_i$) with respect to $\{u\}_i$ such that:

$$\frac{\partial E_{total}}{\partial \{u\}_i} = \sum_{j \neq i}\left[\frac{\partial F}{\partial \rho_i}\frac{\partial f}{\partial r_{ij}} + \frac{\partial F}{\partial \rho_j}\frac{\partial f}{\partial r_{ij}} + \frac{\partial \phi}{\partial r_{ij}}\right] - \{F\}_i = \{0\} \tag{8}$$

Equation (8) expresses the equilibrium equation at atom $'i'$, which represents the equilibrium of the forces acting on atoms $'i'$.

The unbalance force, $\{\xi\}_i$, can then be defined as:

$$\{\xi\}_i = \sum_{j \neq i}\left[\frac{\partial F}{\partial \rho_i}\frac{\partial f}{\partial r_{ij}} + \frac{\partial F}{\partial \rho_j}\frac{\partial f}{\partial r_{ij}} + \frac{\partial \phi}{\partial r_{ij}}\right] - \{F\}_i \tag{9}$$

In order to solve this nonlinear equilibrium equation in an efficient iterative way, it is necessary to differentiate $\{\xi\}_i$ with respect to $\{u\}_i$, i.e.

$$d\{\xi\}_i = \left\{ \begin{array}{c} \dfrac{\partial^2 F}{\partial \rho_i^2}\left(\sum_{j\neq i}\dfrac{\partial F}{\partial \rho_i}\dfrac{[B]}{r_{ij}}\right)\left(\sum_{j\neq i}\dfrac{\partial F}{\partial \rho_j}\dfrac{[B]^T}{r_{ij}}\right) \\[2em] + \sum_{j\neq i}\left\{\left(\dfrac{\partial F}{\partial \rho_i}+\dfrac{\partial F}{\partial \rho_j}\right)\left[\left(\dfrac{\partial^2 f}{\partial r_{ij}^2}-\dfrac{1}{r_{ij}}\dfrac{\partial f}{\partial r_{ij}}\right)[B][B]^T+\dfrac{1}{r_{ij}}\dfrac{\partial f}{r_{ij}}[I]\right]\right\} \\[2em] + \sum_{j\neq i}\left[\left(\dfrac{\partial^2 \phi}{\partial r_{ij}^2}-\dfrac{1}{r_{ij}}\dfrac{\partial \phi}{\partial r_{ij}}\right)[B][B]^T+\dfrac{1}{r_{ij}}\dfrac{\partial \phi}{r_{ij}}[I]\right] \end{array} \right\} d\{u\}_i \quad (10)$$

$$= [K_T]_i \, d\{u\}_i$$

Subsequently, the conventional finite element formulation assembly procedure can be employed to assemble Equation (8) in order to obtain the total system equation, i.e.

$$d\{\xi\} = [K_T]d\{u\} \quad (11)$$

Similarly, Equation (7) can be assembled to obtain the equilibrium equation of the total system, i.e.

$$\sum_i \xi_i = \{f\}_{\text{internal}} - \{F\}_{\text{external}} = \{0\} \quad (12)$$

In terms of the finite element formulation, Equation (11) represents the tangent stiffness equation, while the terms $\{f\}_{\text{internal}}$ and $\{F\}_{\text{external}}$ in Equation (12) denote the internal force vector and the external force vector, respectively. The simulation will adopt the Newton-Raphson iterative technique to solve Equation (12) via the displacement control scheme or force control scheme.

The need to calculate the full matrix of second derivatives in Newton-Raphson method will restrain the size of the simulated system. Therefore, the proposed research will develop an algorithm such as the utilization of the block-diagonal Newton-Raphson method to release this limitation. One of the challenges of nano-scale simulation is to predict the long-time system level performances. Hence, there is an imminent need to develop a multi-scale technique to bridge the gap between nano-scale and micro-scale. In this follow-up project, the proposed research

will develop a coarse graining technique for the multi-scale simulation.

II. Thin Films Study

For the simulations of nano-scale thin film nanoindentation, the simulated system configurations include a perfect three-dimensional crystalline slab of atoms with a (001) surface, and an indenter has a triangular pyramidal form. In the simulation, it is assumed that the hardness of the indenter's diamond tip far exceeds that of the thin copper film. Hence the indenter deformation may be neglected during the indentation process. The simulation assumes boundary conditions in which the atoms located at the four sides and base of the simulated film are fully constrained. The interatomic potential of the substrate is modeled using the Sutton-Chen potential , which has the same functional form in an EAM potential as follows:

$$U = \sum_i U_i \tag{13}$$

$$U_i = \frac{1}{2}\sum_{j \neq i}\phi(r_{ij}) + F(\rho_i) = \varepsilon\left(\frac{1}{2}\sum_{j \neq i}\left(\frac{a}{r_{ij}}\right)^n - c\sqrt{\rho_i}\right) \tag{14}$$

where ρ_i is an electron density-like term for atom i, which is defined as:

$$\rho_i = \sum_{j \neq i} f(r_{ij}) = \sum_{j \neq i}\left(\frac{a}{r_{ij}}\right)^m \tag{15}$$

where r_{ij} is the distance between atoms i and j. The potential between the carbon and copper atoms is simulated using the Born-Mayer potential, which only produces an impulsive force. This potential has the following form:

$$\phi(r_{ij}) = A \exp[-2\alpha(r_{ij} - r_0)] \tag{16}$$

where r_{ij} is the distance between carbon atom i and substrate atom j. This modified-FEM approach is used to perform simulations of nanoindentation. The distribution of the resulting stress and strain is then examined to clarify the atomic plastic behavior induced during the nanoindentation cycle. We will also perform

experiments using depth-sensing indentation technique. The load-depth curves of the experiments will be compared with those of computer simulation by the proposed approach. The indentation size effect and void effect are explored and discussed.

III. Nanotubes Study

The proposed research employs the Tersoff–Brenner many-body potential [39-41] to describe the inter-atomic forces, elastic properties, molecular bond energies, and bond lengths of the nanotubes. It has been used successfully by several researchers to model straight carbon nanotubes and to generate accurate predictions of the thermal properties of carbon nanotubes. The Tersoff–Brenner many-body potential is taken to have the form:

$$E = \sum_i E_i = \frac{1}{2}\sum_{i \neq j} V_{ij} \tag{17}$$

$$V_{ij} = f_c(r_{ij})[V_R(r_{ij}) + b_{ij}V_A(r_{ij})] \tag{18}$$

Here, E is the total energy of the system, which is decomposed for convenience into site energy E_i and a bond V_{ij}. The indices i and j run over the atoms of the system, and r_{ij} is the distance from atom i to atom j. The cutoff function, $f_c(r_{ij})$), is simply taken as

$$f_c(r) = \begin{cases} 1, & r < R - D \\ \frac{1}{2} - \frac{1}{2}\sin\left[\frac{\pi}{2}(r-R)/D\right], & R - D < r < R + D \\ 0, & r > R + D \end{cases} \tag{19}$$

which has continuous value and derivative for all r, and goes from 1 to 0 in a small range around R. R is chosen to include only the first-neighbor shell for most structures of interest. The short range of the potential is numerically advantageous in many applications, and is important for the applicability of the simple ideas about coordination discussed here.

The potential itself contains a repulsive and an attractive part, V_R and V_A, that both have the exponential:

$$V_R(r) = A \exp^{-\lambda_1 r} \tag{20}$$

$$V_A(r) = B \exp^{-\lambda_2 r} \tag{21}$$

In the present work, b_{ij} is taken to have the following from:

$$b_{ij} = (1 + \beta^n \xi_{ij})^{-1/2n} \tag{22}$$

where

$$\xi_{ij} = \sum_{k \neq i,j} f_c(r_{ik}) g(\theta_{ijk}) \exp[\lambda_3^3 (r_{ij} - r_{ik})^3] \tag{23}$$

$$g(\theta_{ijk}) = 1 + \frac{c^2}{d^2} - \frac{c^2}{[d^2 + (h - \cos\theta_{ijk})^2]} \tag{24}$$

where b_{ij} measures the relative strength of the attraction between atoms i and j, which depends on the parameters β and n, and the function, ξ_{ij}, which measures the total effect of all nearby atoms on the interaction. The $f_c(r_{ij})$ is again used to remove the effect of the more distant atoms from the calculation and the angular positions of the atoms are modeled with the function, $g(\theta_{ijk})$, where θ_{ijk} is the angle between atoms j and k, measured from atom i, and the parameters A, B, λ_1, λ_2, λ_3, c, d and h are determined through fitting to experimental data.

The proposed research will systematically establish the atomistic representation of the AFM-tip deformation and develop a detailed definition of the mechanical properties of empty and encapsulated nanotubes during the nanoindentation process. This study will improve the experimental setup of Tombler *et al.* [42] by simulating the nanoindentation of a C_{60}-filled SWCNT suspended between two rigid supports by an atomically sharp tip. The C–C interactions within the nanotube walls are simulated using the Tersoff potential. Meanwhile, the Lennard-Jones (L-J) potential [43] is used

to model the C_{60}–carbon and the C_{60}–C_{60} interactions. Further, we will study the influence of nanotube's diameters and wrapping angles on the mechanical properties of the CNT under nanoindentation. Additionally, this investigation will also consider the effects of temperatures and various C_{60}-densities on the mechanical properties of the filling nanotubes.

Results and Discussion

The nanoindentation size effect

Many investigations into the indentation size effect in metals, indicating that the hardness increases with a decreasing indentation depth, particularly for indentation in the sub-micrometer regime. In these studies, the authors generally apply strain gradient theory to rationalize the indentation depth dependence. The results show that the increase in hardness is inversely proportional to the square root of the indentation depth. In this regard, the indentation size effect is similar to the Hall-Petch relationship describing the grain size effect on the strength of metals and alloys. However, the Hall-Petch equation does not apply at the nanoscale, as indicated by Schietz and Jacolosen (*Science*, 2003) that conducted molecular dynamics (MD) simulations and showed that the strength of copper does not retain size dependence when the grain size falls to the nanometer scale. Accordingly, this study is to investigate the validity of this phenomenon in the nanometer regime. Static atomistic simulations, based on an energy minimization formulation, are performed to analyze the depth dependence of nanohardness. This approach is unique in that not only does it utilize the fact that the equilibrium position of the atoms of the condense matters is its minimum energy position but is also uses the FEM formulation to make the computational process efficient.

In this manner, we evaluate the nanohardness for spherical indenter and pyramidal indenter indentations with $4\overset{o}{A}$, $7\overset{o}{A}$, and $10\overset{o}{A}$ indentation depths as listed in the Table 1. In nanoindentation tests, the contact depth (h_c) is estimated from total indentation depth (h_t) by

$$h_c = h_t - \varepsilon P_{\max} / S_{\max} \qquad (25)$$

where ε=0.72 for pyramidal indenter, ε=0.75 for spherical indenter, and $S_{\max}$ is the stiffness, equal to the slope of the unloading curve (dp/dh) at the maximum load ($P_{\max}$). The projected contact area is then obtained by the project contact area-to-contact depth relationship from the indenter geometry. We also utilize the load/depth curves obtained from simulations to determine the nanohardness by the analysis procedure described above. The calculated values are also listed in the Table 1. Table 1 shows that the nanohardness values calculated using equation (13), especially for pyramidal indenter, are much higher than those calculated using the true contact area identified by the contact pressure. Hence, equation (13) significantly underestimates the contact depth estimated in all of the simulation cases. That is, nanohardness does have strong depth dependence for pyramidal indenter indentation if Oliver-Pharr method is adopted.

In order to check the validity of the Oliver-Pharr method further, we utilize the simulated atomic configuration to calculate the contact pressure distribution under the indenter and inter-atomic sliding by slip vector analysis [6]. Figure 2 shows the top views for the distributions of (a) the contact pressure and (b) slip vector norm under pyramidal-indenter at the maximum indentation depth of $7\overset{o}{A}$. Based on continuum mechanics, Cheng et al. [19] conducted a series of finite element analyses to check the validity of the Oliver and Pharr method. Their study concluded that the method underestimates the contact area for elastic-perfectly plastic solids for most materials.

Similarly, it can be seen in Figure 2 that for most atoms in the contact area, there is relative sliding between them that is, plastic deformation occurred and no obvious strain hardening observed from the distribution of the contact pressure under the indenter. From these results, it may be concluded that the commonly used Oliver-Pharr method is not valid any more as the indentation depth goes into nanometer regime.

From the definition of hardness adopted in this paper, it is quite intuitive to interpret hardness as mean contact pressure physically. Figure 3 shows the distributions of the contact pressure under pyramidal-indenter at the maximum indentation depth of (a) $4\overset{o}{A}$, (b) $7\overset{o}{A}$, and (c) $10\overset{o}{A}$. Indeed, in comparison with the hardness values listed in Table 1, hardness value represents mean contact pressure using the contact area identified by the contact pressure. As described in the strain gradient theory of previous studies, the indentation size effect is correlated to the density of geometrically necessary dislocations that induces large strain gradient in turn. Therefore, we calculate the strain gradient at three different indentation depths to check whether the strain gradient varies increasingly with decreasing indentation depth. Figure 4 shows the distributions of the strain gradient on the surface under the pyramidal indenter of the copper substrate for three different depths. From Figure 4, it is obvious that there is no increasing trend for strain gradient for decreasing indentation depth. Moreover, Chiu et al. [20] utilized TEM to measure the plastic zone induced during nanoindentation on $Ni_3Al(Cr, B)$ single crystal. Their research showed that nanohardness is fairly constant with respect to the load if nanohardness is determined by dividing the load by the projected area of the plastic zone.

Figure 5(a) presents the variation in the load (i.e. the force experienced by the indenter) with the indentation depth for nanoindentation cycles performed with no

15

void and with voids of three different sizes, respectively. Meanwhile, Figure 5(b) shows the load-depth curves for nanoindentation cycles performed with no void and with voids positioned at three different depths within the Cu slab, respectively. Figure 5(a) demonstrates that, compared to the no void case, the presence of a void of any size leads to an enhanced displacement burst at an indentation depth of 0.55 nm and a 10~15 % reduction in the magnitude of the maximum load. Figure 5(b) shows that the reduction in the maximum load is larger when the void is located closer to the free surface, i.e. the void depth is smaller. For the minimum void depth of 1.0 nm, the displacement burst is activated at a smaller indentation depth and results in the greatest load reduction. Having evaluated the contact pressure from Eq. (13), the true contact area can be accurately determined and the nanohardness obtained. Table 2 lists the maximum loads and nanohardnesses obtained for the different void parameters considered in the present simulations. The nanohardness is computed by dividing the maximum load by the projected area of contact at that load. Table 2 demonstrates that a larger maximum load always corresponds to a larger nanohardness for the current simulation conditions. Hence, it can be concluded that the contact area is not influenced significantly by the presence of a void.

Figure 6 shows the distributions of the hydrostatic stress and the von Mises stress induced at the maximum indentation depth in the cross-section of the indented copper substrate through the indenter tip and parallel with the (-1 01) plane. The results correspond to the case of no void and to the case of a void with a diameter of 1.2 nm and a depth of 1.5 nm. A comparison of the four subplots reveals that the distribution of the von Mises stress is not affected significantly by the presence of a void. However, the void does have a significant influence on the distribution of the hydrostatic stress. It can be seen that the stress accumulates at the internal surface of the void causing a reduction in the contact pressure.

16

Figure 7 presents the distributions of the hydrostatic stress for two different void parameters in the same cross section as Figure 6. Subplots (a)~(c) reveal the variation of the hydrostatic stress distribution with the void size, while subplots (d)~(f) illustrate the variation of the hydrostatic stress distribution with the void depth. It is observed in subplots (a) and (d) that although the void disappears, a stress concentration remains at the original void location. The disappearance of the void is to be expected since in these two cases, the indentation depth is sufficiently large to cause many surrounding atoms to slip into the void vacancy. The remaining subplots of Figure 7 all reveal that stress accumulates at the internal surface of the void. The stress accumulation causes a reduction in the contact pressure and prompts the void to deform into an elliptical shape. A stress reduction in the contact area is consistent with the maximum load reduction observed when a void exists in the substrate.

In order to explore the influence of a void on the deformation mechanisms in nanoindentation, the dislocation structure in the substrate can be analyzed by performing a slip vector calculation at each atomic site. This quantity gives the Burgers vector for the slip of adjacent atomic planes, where the atom lies on one of these planes. It has a large magnitude for any inhomogeneous deformation near an atom and provide information regarding the deformation.

Results show that the observed dislocation structures resemble four-sided pyramids, whose sides lie parallel to the four different sets of {111} planes. This finding is reasonable since slip is known to occur along the close-packed {111} planes in FCC crystalline structures. The slip vector norms indicated in green correspond to 1.47 A, which is very close to the value of a <112> partial dislocation in copper. Furthermore, the slip vector norm value of the atoms indicated in red is 2.56 A, which is consistent with the magnitude of a <110> perfect dislocation.

Furthermore, results show that the dislocation structure is not influenced

significantly by the presence of a void. This finding provides a reasonable explanation for the earlier conclusion that the contact area is unaffected by the existence of a void.

Contact behavior and tribological phenomena of nano-scale interfaces

In the micro- or nano-scale domains, the initial contact between two bodies takes place between the asperities on their surfaces. Unlike nanoindentation processes performed using hard indenters in which deformation is confined primarily to the substrate, contact between two micro- or nano-scale bodies results mainly in a deformation of the surface asperities. When two rough surfaces contact one another, the load is borne by the tips of the surface asperities, and thus the actual contact area is only a small fraction of the apparent contact area. So far continuum contact mechanics has been used to quantify the contact behavior at the nano-interfaces. However, the applicability of continuum mechanics to such interfaces is unclear. The proposed research will utilize a FEM atomic model to investigate the contact behavior at nano-scale interfaces.

As shown in Figure 8, the simulation model comprises two parts, namely a rigid carbon plate and a deformable copper substrate containing cubic (0 0 2) planes of dynamic atoms supporting an asperity with a diameter of 150Å. Periodic boundary conditions are imposed in the [1 0 0] and [0 1 0] directions to overcome the problem of size effects. To achieve a realistic asperity configuration, the asperity is first constructed on the substrate surface and is then thermally annealed. The rigid carbon plate is moved incrementally in the downward direction such that it impresses the copper asperity. Following each displacement of the rigid plate, the energy of the entire system is minimized using the block-diagonal Newton-Raphson method to achieve equilibrium conditions.

Figures 9(a) and 9(b) illustrate the variations of the dimensionless contact area and the dimensionless contact load, respectively, with the dimensionless interference between the rigid plate and the copper substrate supporting the asperity. In both figures, the results obtained from the current static atomistic simulations are compared with those obtained from the perfectly-elastic Hertzian contact model and three elastic-plastic models, namely the CEB, ZMC and KE models. From Figure 9(a), it can be seen that when $\omega < \omega_c$, all of the models converge to the GW model and exhibit a Hertzian elastic solution. However, as the plasticity increases, the discrepancy between the results of the various models also increases. It is observed that the contact area predictions of the CEB model are consistently higher than those of the current model with the dimensionless interference (ω/ω_c). This result is to be expected since the CEB model treats the elastoplastic contact by modeling a plastically deformed portion of a hemisphere using volume conservation and therefore overestimates the contact area as soon as the point of critical interference is reached, i.e. $\omega/\omega_c > 1$. By comparison, the contact area predictions of the ZMC model are lower than those of the current static atomistic model at small values of interference, i.e. $\omega/\omega_c = 10$, but are higher than those of the current model at interferences greater than $\omega/\omega_c = 51$. Furthermore, it is observed that the contact area predictions of the ZMC and CEB models are equal when the interference has a value of $\omega/\omega_c \geqq 54$. This result arises because the contact area is calculated from the geometrical intersection of the flat surface with the original profile of the sphere in accordance with the fully plastic model.

In this study, the results of Figure 9(a) reveal that if the upper surface in the contact pair is extremely smooth such that the deformation behavior of the compressed asperity transits from elastic to elastic-plastic to plastic deformation,

respectively, the results obtained using the current static atomistic simulations for the dimensionless contact area are in good general agreement with the predictions of existing continuum mechanics. Figure 9(b) illustrates the results obtained by the various models considered above for the variation of the contact load (P/P_c) with the interference (ω/ω_c). It is evident that the contact load predicted by the CEB model deviates significantly from that predicted by the current static atomistic model; particularly at larger values of the interference, i.e. ω/ω_c=23. This discrepancy arises as a result of the inappropriate assumption of a constant mean pressure in the CEB model and an overestimation of the contact area, as shown in Figure 9(a). It is observed that the contact load predictions of the current model are closer to those of the ZMC model than those of the CEB scheme at larger values of the interference, i.e. ω/ω_c=33. It can also be seen that the contact load predictions obtained from the current static atomistic model are in excellent agreement with the results generated by the KE model. However, at high values of the interference, the static atomistic simulation results have a significant deviation of the contact load. (Note that for reasons of clarity, the deviation of the contact load at higher values of the interference do not appear within Figure 9(b)). In this regard, the results of the current model are in agreement with those of the FEM model presented by Jackson *et al.* [41], in which the effects of the deformed geometry in the contact regime are taken into account. The significant deviation of the contact load can be attributed to the fact that the asperity is not hemispherical (particularly after the elastoplastic contact which occurs during the loading process) since the initial point of contact lies much closer to the flat surface as the asperity contact evolves into an elastoplastic contact.

In order to explore the effect of the contact depth on the contact stress induced in the single asperity, Figure 10 illustrates the distribution of the contact load on a typical single asperity at various contact depths of 8, 16 and 24 Å. In general, at a low

contact depth, the spherical asperity deforms only elastically. While in this elastic regime, the maximum stress is generated beneath the contact surface and is located within the asperity itself. However, as the interference increases, the magnitude of the stress also increases, leading to a yielding effect at the point of maximum stress. At contact depths just beyond this point (defined as the critical point), plastic deformation takes place within a small region of the asperity. As indicated in Figure 10(a), this region of plastic deformation is small and is confined below the asperity surface by a sizable region of elastic material. However, when the region of plastic deformation extends as far as the asperity surface, an elastic volume is still maintained on the loaded tip of the asperity as a result of hydrostatic stresses [see Figure 10 (b)]. As the level of interference is increased further, this elastic region transforms into a plastic region, which expands until it reaches the edge of the asperity (see Figure 10 (c)). Significantly, the results presented in Figure 10 reveal that the predicted stress distribution is highly sensitive to variations in the contact interference. This is most likely a result of a centralization of the stresses in the contacting surfaces.

The simulation results obtained for the variations of the contact area and contact load with the level of contact interference are in good agreement with those predicted by the Hertzian continuum model at small levels of interference. When the mechanical contact behavior of the single asperity develops from fully elastic through elastic-plastic to fully plastic contact interface, the current predictions for the contact area and contact load are higher than those generated by the fully-plastic model. Importantly, the current simulation results for the contact area and contact load are in close agreement with those predicted by continuum theory in the elasto-plastic and plastic regimes.

21

Nanotube

This project also commences by performing the experimental nanoindentation tests to investigate the buckling mechanism of nanotube probes under an axial compression load. The carbon nanotube used in the nanoindentation tests are fabricated using a conventional dc arc-discharge method [42]. The carbon nanotube probes used in the nanoindentation tests [Figure 11(a)] are fabricated by attaching individual nanotube to an indenter tip using electrophoresis [43] and electrostatic techniques [44]. Nanoindentation tests were performed using a Veeco/TM multimode nanoindentation device operating under the control of CP RII SPM controller. In general, nanotube probes are slender, thin-walled structures. Consequently, they are highly susceptible to buckling when loaded in compression or bending. Buckling results in a sudden reduction in the load which the nanotube can support, and frequently leads to the catastrophic failure of nanotubes. For long nanotubes ($L/d{\sim}100$, where L and d are the length and diameter, respectively), axial compression results in "Euler-buckling" [Figure 11(b)]. Conversely, short nanotubes ($L/d{\sim}1{-}20$), undergo "post-buckling" [Figure 11(c)].

Figures 12 show the experimental force-displacement curves obtained from nanoindentation tests performed using CNTs of lengths 300 and 100 nm, respectively. In the case of the longer tube [Figure 12(a)], it can be seen that the force initially linear increases with an increasing displacement. At a certain displacement, a discontinuity is formed in the curve, following which a significant increase in the displacement occurs with no obvious change in the force. Transitioning from the linear rise to the force plateau involves some softening, indicated by the rounding in the curve. For the shorter nanotube [see Figure 12(b)], the flat plateau is replaced by a sharp decrease in slope and this plateau results in relative stiffening of the nanotube

due to the deformation-promoted reactivity [45]. This phenomenon is most likely attributed to buckling instabilities of the nanotube associated with a release of the local compressive stress. The appearance of this plateau is significantly repeatable in the case of the short sample and we interpret it as global-buckling in nanotubes. A similar observation is consistent with the findings presented in a previous study into an array of multi-walled carbon nanotubes (MWCNTs) under nanoindentation [46]. Here, the critical loads (f_{cr}) of nanotube of 100nm and 300nm have been measured to be 16.15 μN and 12.96μN, respectively. The critical load for a classical elastic column, if MWCNTs behave like elastic cylinder, is often called critical load and given by [47]:

$$f_{cr} = \pi^2 YI/L_e^2 \qquad\qquad (26)$$

where Y is the Young's modulus and $I = \pi(R_2^4 - R_1^4)/4$ is the moment of inertia of the MWCNT with inner and outer radii of R_1 and R_2, respectively. The effective length L_e is expressed in term of an effective-length factor K by: $L_e = KL$, where L is the actual length of the nanotube. Buckling behavior of nanotube in this work can be approached by two possible conditions as follows: (1) $K=2$, a nanocolumn fixed at the top and free at the base is called a fixed-free column, where $f_{cr} = \pi^2 YI/(4L^2)$; (2) $K=0.7$, a nanocolumn fixed at the top and pinned at the base is called a fixed-pinned column, where $f_{cr} = 2.046\pi^2 YI/L^2$. As shown in Table 3, we can estimate critical stress (σ_{cr}), critical buckling strain (ε_{cr}), and Young's modulus of nanotubes by critical buckling load of individual nanotube. It should note that the value of Young's modulus for carbon fibers is about 0.68 TPa [48], and smaller than the values of CNTs. Based on Euler buckling, it has been found that the Young's modulus of nanotube depends on lengths and diameters and whether we evaluate the ones by fixed-free column or fixed-pinned column mode. This behavior can be attributed to high internal stress resulting from the surface stress and high aspect ratio at the nanoscale. Our

experimental results show that longer nanotubes buckle in local-buckling mode, whereas shorter nanotubes undergo global-buckling.

Having completed the experimental nanoindentation, this study performed a series of MD simulations to evaluate the effect of nanotube lengths and initial inclination angles on buckling behaviors as the nanotube probe was compressed into contact with a silicon substrate. Figure 13 presents a schematic representation of the simulation model. Because CNTs with experimental sizes could not be simulated due to computational power limits, smaller nanotubes (i.e., 11.6–19.4 nm in length and 1.36 nm in diameter) were deliberately considered instead in order to focus on the length effect on buckling behaviors of CNTs themselves. Although MWCNTs were used in the current experiment, our simulation assumes that buckling behaviors of CNTs may approach that of single-walled carbon nanotubes (SWCNTs) with a radius equal to the average radius of MWCNTs when the nanotube wall thickness is small compared to its radius. Tersoff potential [39-41] has been applied in present CNT probes. Additionally, the interactions between the CNT probe and the Si substrate are modeled using the L-J potential [43]. In this simulation, the nanotube is inclined at a small angle (θ) from the vertical in order to reflect the physical case [52] where the nanotube is inclined toward one side of the pyramidal indenter tip following its attachment, where the loading (unloading) during the indentation process was performed with a time step of 0.15 fs. Figure 14(a) plots the variation of the strain energy per atom with the downward indenter displacement for CNTs of lengths 11.6, 13.2, and 19.4 nm, respectively, and initial inclination angles of $\theta=5°$ and $\theta=12°$. Fig. 14(b) presents snapshots of nanotubes of length 19.4 nm with initial inclination angles of $\theta=5°$ [upper Figure 14(b)] and $\theta=12°$ [lower Figure 14(b)]. During the initial approach of the nanotube toward the Si surface [snapshots (A) and (a) in Fiure 14(a)], an attraction occurs (i.e. negative energetic) due to van der Waals forces between the

end of the nanotube and the substrate surface. This attraction causes a significant reversal until the point where the van der Waals forces become repulsive [snapshots (B) and (b) in Figure 14(a)]. This phenomenon is in good agreement with the results reported by Garg *et al.* [53]. The Young's modulus of each CNT can be calculated as the second derivative of the total energy with respect to downward displacements at the equilibrium configuration [54], i.e.

$$Y = \frac{1}{V_0} \left(\frac{\partial^2 E}{\partial \varepsilon^2} \right)_{\varepsilon=0} \tag{27}$$

where V_0 is the equilibrium volume, ε is the strain (i.e. $\varepsilon = D/(L\cos\theta)$, where D is the downward displacement of indenter), and E is the total energy. Although establishing the exact Young's modulus is difficult due to the a few changes in the second derivative, we have simply indicated that structural instability by a sudden turning point in the internal energy of carbon atoms and calculated the mechanical properties of CNTs. A similar technique has also been utilized to investigate the mechanical responses of nanotubes by Xiao *et al.* [55] and Seifert *et al.* [56]. Applying Eq. (27) and assuming a wall thickness of 3.4 Å, Young's moduli of CNTs of lengths 11.6, 13.2 and 19.4nm are found to be 1.213, 0.987, and 0.865 TPa, respectively. Furthermore, to develop further insights into buckling instabilities of nanotube probes, the deformation of CNTs has been considered from the continuum theory based on Eq. (26). Table 4 shows that the number of buckles, and provides reasonable critical loads when buckles are available to the two types of boundary condition (i.e., the fixed-free and fixed-pin compression cases) under nanoindentation. The present results indicate that the critical buckling force and the number of buckles are sensitive to the lengths of CNTs. Figures. 14(a) and 14(b) also show that the longer nanotubes at a constant initial inclination angle (θ=5°) not only experience a greater total number of buckles than shorter nanotubes, but also has the onset of buckling at a relatively lower

25

displacement. The difference in the structural evolution of nanotubes can be attributed to the fact that longer nanotubes are liable to "slipping" or "flattening" effects. A similar observation was also noted by the computational study into the compression of SWCNTs by Wang *et al.*[57]. It can also be seen that the critical buckling force significantly decreases as the initial inclination angle increases. Specifically, at smaller inclination angles, the nanotube tends to buckle in a global manner, i.e. global-buckling, while at higher inclination angles, the nanotube tends to buckle in a local-buckling.

Our experimental and theoretical results present a valuable insight into the buckling instability of nanotube probes. This study has shown that longer nanotubes buckle in local-buckling, whereas shorter nanotubes undergo global-buckling. The simulation results suggest that, for a lower inclination angle, the nanotubes may exhibit global-buckling. However, for higher inclination angles, the nanotubes buckle in local-buckling.

Effect of adsorbed layers in ultra-low depth nanoindentation

This project performs theoretical and experimental investigations to examine the changes induced in the mechanical properties of a nanoindented thin copper (Cu) film by the presence of an adsorbed layer on its surface. As shown in Figure 15, the simulation model comprises a perfect three-dimensional crystalline slab of Cu atoms with a (001) surface and dimensions of 14.5 nm $\times$14.5 nm $\times$6 nm, a thin polymer adsorbed layer and a diamond (C) indenter. The C-C interactions within the diamond indenter are simulated using the Tersoff potential [39-41], while the Cu-Cu interactions within the Cu sample and the interactions between the Cu sample and the indenter are both modeled using the Morse potential [56]. Finally, the intramolecular behavior of the polymer adsorbed layer is described using the finitely extendable

nonlinear elastic (*FENE*) potential and the L-J potential. These potentials have been widely applied in previous molecular dynamics simulations of polymer-based systems [37, 57-60]. The loading (unloading) steps of the indentation process are simulated using a time step of 0.5 fs and the *NVT* model [61] is employed to control the number of atoms *N*, the volume *V* and the temperature *T* of the simulation system. In order to clarify the effects of the adsorbed layer thickness on the mechanical properties of the thin Cu film under nanoindentation, the simulations are performed using polymer adsorbed layers of various thicknesses ranging from 3 to 9 Å with the constant force of 150 nN. As shown in Figure 16, it is apparent that the thickness of the adsorbed layer has a direct effect on the initial slope of the load-displacement curves of the various Cu samples. Specifically, the slope decreases with an increasing adsorbed layer thickness. This phenomenon arises as a result of a greater number of polymer entanglements as the adsorbed layer thickness increases, which in turn decreases the elastic stiffness of the Cu specimen. It is also observed that for a constant indentation force, the indentation depth reduces as the adsorbed layer thickness decreases, which implies that the mechanical strength of the Cu samples increases with a reducing adsorbed layer thickness. This observation can be attributed to the fact that the presence of the polymer adsorbed layer reduces the adhesion force between the indenter and the workpiece. Therefore, upon unloading, less elastic recovery occurs within the indented penetration zone and hence the shape of the indentation feature following complete unloading is similar to that formed at the maximum indentation depth.

To further illustrate the effects of the adsorbed layer on the structural deformation of the Cu samples, Figure 17 presents atomic configuration models which clearly show the formation of significant slip planes (indicated by the red arrows) during the unloading stage. All three figures show the presence of slip planes

aligned in the direction of the side faces of the pyramidal indenter. In general, as the indenter is pushed into the Cu sample, local polymer molecules become trapped at the indentation interface, thereby forming a cavity on the Cu surface. During the subsequent unloading stage, the polymer molecules remain trapped within the Cu substrate and thus the cavity grows, resulting in the formation of a rough residual indentation mark and prompting the onset of slip planes along the edges of the indenter. However, when the substrate has no polymer adsorbed layer, the upper layer of the Cu substrate remains in constant contact with the indenter during nanoindentation. Following the unloading stage, the residual indentation mark is found to have a relatively shallower penetration than that observed in the specimen with an adsorbed layer as a result of recrystallization and elastic recovery induced by the adhesion between the indenter and the Cu substrate. Therefore, as shown in Figure 16, for a constant load, the indentation depth increases with an increasing adsorbed layer thickness. Meanwhile, the bonds between the Cu atoms in the substrate and the C atoms in the indenter are weakened as a result of the polymer layer between them, and hence a poorer elastic recovery takes place. In other words, the microstructural damage caused to the Cu substrate during the nanoindentation process becomes more severe as the adsorbed layer thickness increases. The slip planes observed in Figures 17(a)~(c) are in marked contrast to the local pile-up or sink-in surface distortion effects observed on a pure indented Cu surface. Overall, the results presented in Figures 16 and 17 imply that the presence of an adsorbed layer reduces the mechanical strength of the indented specimen, particularly for indentation depth in the nanometer regime. As a result, it can be inferred that the yield strength and hardness values computed in conventional MD studies for ultra-low depth nanoindentation will be overstated unless the effect of the adsorbed layer in reducing the adhesion force between the indenter and the workpiece is taken into account.

Conclusion

The proposed program is an integrated project to conduct concerted team effort for the quantification of nano-material systems. This research has studied the mechanical property of nano-scale thin films and nanotubes.

Our simulation results show that the nanohardness does not have strong dependence of the indentation depth when the indentation depth falls into the nanometer regime. In other words, the nanohardness depth dependence has limit in the nanoscale regime. It is also concluded that the nanohardness is overestimated significantly using the analysis procedure commonly adopted in the nanoindentation testing. That is, the Oliver-Pharr method representing elastic-plastic continuum contact model does not work in the nanometer regime any more. This project has presented static atomistic simulations of the previously unexplored question of how nanoindentation is influenced by the presence of a void. Stress analysis has explained the observed reduction in maximum load caused by a void. Meanwhile, observation of the dislocation structure by means of slip vector analysis has shown that deformation in nanoindentation is not influenced significantly by the presence of a void. However, the cases simulated in this study have revealed that the existence of a void causes a reduction in the magnitude of the nanohardness by the order of approximately 10~15 %. Furthermore, we also employs an atomic FEM model to investigate the mechanical contact behavior of a single asperity. The results are compared with those obtained from continuum models such as the CEB, ZMC and KE models. The results obtained from the current model for the relationships between the mean contact pressure and contact area, respectively, and the contact interference are found to be in good agreement with the predictions yielded by continuum theory as the mechanical contact behavior of the asperity transits through two distinct stages ranging from fully

elastic to an elastoplastic contact interface.

In this project, our experimental and theoretical results present a valuable insight into the buckling instability of nanotube probes. This study has shown that longer nanotubes buckle in local-buckling, whereas shorter nanotubes undergo global-buckling. The simulation results suggest that, for a lower inclination angle, the nanotubes may exhibit global-buckling. However, for higher inclination angles, the nanotubes buckle in local-buckling.

In addition, this project has performed a series of MD simulations and experiments to investigate the effects of adsorbed layers on the mechanical properties of thin films under ultra-low depth nanoindentation. Our Findings have shown that the mechanical strength of the thin film reduces as the thickness of the adsorbed layer increases, particularly for indentation in the nanometer regime. Furthermore, the results also imply that the predicted values for the mechanical properties of thin films under nanoindentation will be overestimated if the simulations fail to take account of the effect of the adsorbed layer in weakening the bonds between the indenter and the substrate.

References

[1] Iijima S 1991 Nature **354** 56

[2] Iijima S and Ichihashi T 1993 Nature **363** 603

[3] Ajayan P M and Ebbesen T W 1997 Rep. Prog. Phys. **60** 1025

[4] Ebbesen T W (ed) 1997 Carbon Nanotubes, Preparation and Properties (Boca Raton, FL: CRC Press)

[5] Wang Z L, Poncharal P and de Heer W A 2000 J. Phys. Chem. Solids **61** 1025

[6] Sishen Xi, Wenzhi L, Zhengwei P and Baohe C 2000 J. Phys. Chem. Solids **61** 1153

[7] Bethune D S, Kiang C H, Devries M, Gorman G, Savoy R, Vazquez J and Beyears R 1993 Nature **363** 605

[8] Thess A et al 1996 Science **273** 483

[9] Chopra N G et al 1995 Science **269** 966

[10] Loiseau A, Willaime F, Demoncy N and Hug G 1996 Phys. Rev. Lett. **76** 4737

[11] Golberg D, Eremets M and Kurashima K 1996 Appl. Phys. Lett. **69** 2045

[12] Bengu E and Marks L D 2001 Phys. Rev. Lett. **86** 2385

[13] Suenaga K, Demoncy N, Loiseau A andWillaime F 1997 Science **278** 653

[14] Rapoport L, Bilik Y, HomyonferM and Cohen S R 1997 Nature **387** 791

[15] Feldman Y, Wasserman E and Srolovitz D J 1995 Science **267** 222

[16] Tenne R, Margulis L, Genut M and Hodes G 1992 Nature **360** 444

[17] Hacohen Y R, Grunbaum E, Tenne R and Hutchinson J L 1998 Nature **395** 336

[18] Cote M, Cohen M L and Chadi D J 1998 Phys. Rev. B **58** 4277

[19] Cheng Y T and Cheng C M 1998 Philos. Mag. Lett. **78** 115

[20] Chiu Y L and Ngan A H W 2002 Acta Mater. **50** 2677

[21] Hamdani F et al 1998 J. Appl. Phys. **83** 983

[22] Huang Y, Duan X, Cui Y and Lieber C M 2002 Nano Lett. **2** 101

[23] Kim J et al 2002 Appl. Phys. Lett. **80** 3548

[24] Joshua G, Rongrui H, Zhang Y and Sangkwon L 2003 Nature **422** 599

[25] Hay, J. L., O'Hern, M. E., Oliver, W. C., 1998, Mat. Res. Soc. Symp. Proc. **522**, 27.

[26] Hay, J. C., Pharr, G. M., 1998, Mat. Res. Soc. Symp. Proc. **522**, 39.

[27] Lucas, B. N., Oliver, W. C., Swindeman, J. E., 1998, Mat. Res. Soc. Symp. Proc. **522**, 3.

[28] Lu, W., Komvopoulos, K., 2001, J. Tribo. **123**, 641.

[29] Perez, R., Payne, M. C., Simpson, A. D., 1995. Phys. Rev. Lett. **75**, 4748.

[30] Zimmerman, J. A., Kelchner, C. L., Klein, P. A., Hamilton, J. C., Foiles, S. M., 2001. Phys. Rev. Lett. **87**, 165507.

[31] Fuente, O. R. de la, Zimmerman, J. A., Gonzalez, M. A., Figuera, J. de la , Hamilton, J. C., Pai, W. W., Rojo, J. M., 2002. Phys. Rev. Lett. **88**, 036101.

[32] Knap, J., Ortiz, M., 2003. Phys. Rev. Lett. **90**, 226102.

[33] Minot, E. D., Yaish, Y., Sazonova, V., Park, J. Y., Brink, M. and McEuen, P. L., 2003. Phys. Rev. Lett. **90**, 156401.

[34] Walters, D. A., Ericson, L. M., Casavant, M. J., Liu, J., Colbert, D. T., Smith, K. A. and Smalley, R. E., 1999. Appl. Phys. Lett. **74**, 3803.

[35] Decossas, S., Cappello, G, Poignant, G., Patrone, L., Bonnot, A. M., Comin, F. and Chevrier, J., 2001. Europhys. Lett. **53**, 742.

[36] B. Bhushan, J. N. Israelachvili, and U. Landman, Nature **374**, 607 (1995)

[37] G. He, M. H. Müser, and M. O. Robbins, Science **284**, 1650 (1999)

[38] G. He and M. O. Robbins, Tribol. Lett. **10**, 7 (2001)

[39] Tersoff, J., 1988. Phys. Rev. Lett. **61**, 2879.

[40] Tersoff, J., 1988. Phys. Rev. B **37**, 6991.

[41] Tersoff, J., 1989. Phys. Rev. B **39**, 5566.

[42] Tombler, T. W., Zhou, C., Alexseyev L., 2000. Nature (London) **405**, 769.

[43] Allen, M. P. and Tildesley, D. J., 1987. *Computer Simulation of Liquids* (Oxford University Press, New York).

[44] Jackson, R. L., Green, I.,2005, ASME J. Tribol. **127**, 343

[45] Ebbesen, T. W., Ajayan, P. M., 1992, Nature **358**, 220.

[46] Yamamoto, K., Akita, S., Nakayama, Y., 1998, J. phys. D: Appl Phys. **31,** 34.

[47] Stevens, R. M. D., Frederick, N. A., Smith, B. L., Morse, D. E., Stucky, G. D., Hansma, P. K.,2000, Nanotechnology **11,** 1.

[48] Mylvaganam, K., Zhang, L. C.,2006, Nanotechology **17,** 410.

[49] Waters, J. F., Guduru, P. R., Jouzi, M., Xu, J. M., Hanlon, T., Suresh, S., 2005, Appl. Phys. Lett. **87,**103109.

[50] Timoshenko, S. P., Gere, J. M., *Theory of Elastic Stability* (McGraw-Hill, New York, 1961).

[51] Jacobsen, R. L., Tritt, T. M., Guth, J. R., Ehrlich, A. C., Gillespie, D. J.,1995, Carbon **33,** 1217.

[52] U. Landman, W. D. Luedtke, N. A. Burnham, and R. J. Colton**,** Science **248**, 454 (1990).

[53] A. Garg, J. Han and S. B. Sinnott, Phys. Rev. Lett. **81** 2260 (1998)

[54] Y. R. Jeng, P. C. Tsai, and T. H. Fang, Phys. Rev. B **74**, 045406 (2006).

[55] T. Xiao and K. Liao, Phys. Rev. B **66**, 153407 (2002).

[56] G. Seifert, E. Hernández, Chem. Phys. Lett. **318** 355 (2000).

[55] Y. Wang, X.X. Wang, and H.A Wu, Comput. Mater. Sci. **32**, 141 (2005).

[56] L. A. Girifalco and V. G.Weizer, Phys. Rev. **3**, 114 (1959).

[57] G. He and M. O. Robbins, Tribol. Lett. **10**, 7 (2001)

[58] H. R. Warner, Jr., Ind. Eng. Chem. Fundam. **11**, 379 (1972)

[59] G. S. Grest and K. Kremer, Phys. Rev. A **33**, 3628 (1986)

[60] Y. R. Jeng, C. C. Chen, and S. H. Shyu, Tribol. Lett. **15**, 293 (2003)

[61] W. G. Hoover, Phys. Rev. A **31**, 1695 (1985)

Table 1. The nanohardness calculated in two methods for two different

indenter geometries at three indentation depths.

Geometry of indenter	Indentation depth h_t ($\overset{o}{A}$)	Nanohardness calculated using the true contact area (GPa)	Nanohardness calculated using equation (5) (GPa)
pyramidal	4	5.1	15.7
pyramidal	7	4.9	11.8
pyramidal	10	4.7	9.5
spherical	4	7.6	8.1
spherical	7	6.2	7.3
spherical	10	6.3	7.8

Table 2.   Nanohardness values for two void parameters (Void Size and Depth).

Void parameters (Size and Depth)	Maximum Load (10 eV/nm)	Nano-hardness (Gpa)
No Void	222	6.27
Size=0.8 nm Depth=1.3 nm	194	5.58
Size=1.2 nm Depth=1.0 nm	183	5.32
Size=1.2 nm Depth=1.5 nm	190	5.52
Size=1.2 nm Depth=2.0 nm	196	5.69
Size=1.6 nm Depth=1.7 nm	182	5.29

Table 3. Critical stress, critical buckling strain and Young's modulus of

nanotubes.

Sample description		σ_{cr} (GPa)	ε_{cr} (%)		Y (TPa)	
			Fixed-free	Fixed-pin	Fixed-free	Fixed-pin
A	Length: 300 nm OD:28 nm ID:10 nm	24.12	0.15	1.24	15.92	1.94
B	Length: 100nm OD:17 nm ID:5 nm	77.89	0.48	3.97	16.09	1.96
	Carbon fibers					0.68[c]

[a] OD: Outer diameter

[b] ID: Inner diameter

[c] Reference 48

Table 4.   Dependence of Young's modului obtained from MD simulations and

the critical buckling load calculated by Eq. (26) with two types of

buckles.

CNT Length (nm)	number of buckles (n)	Critical buckling load (nN)	
		Fixed-free	Fixed-pin
11.6 (θ=5°)[a]	2	14.94	122.32
13.2 (θ=5°)	2	9.39	76.67
19.4 (θ=5°)	2	3.81	31.11
19.4 (θ=12°)	1	0.95	7.78

[a] θ: Initial inclination angles

Figure1   The   atomistic   model   used   in   the   nanoindentation   simulation.

(unit:angstrom)
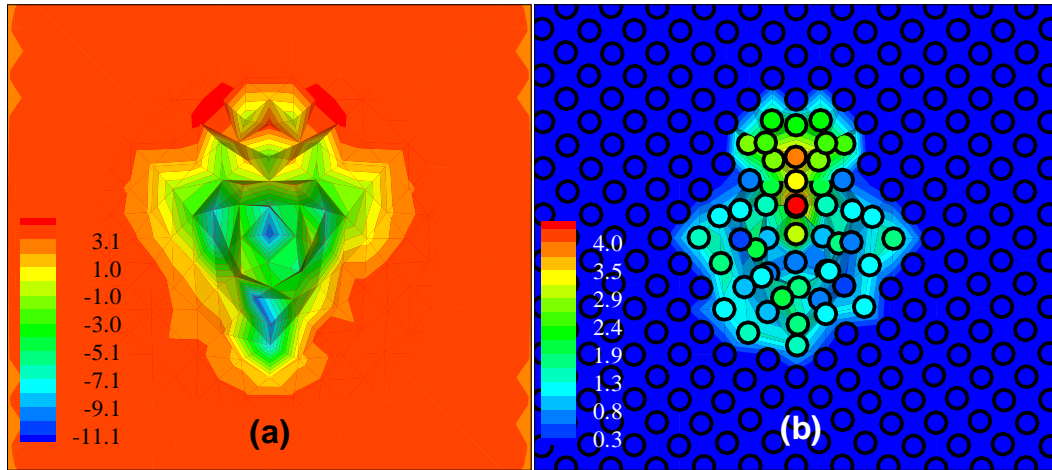
Figure 2 The top views for the distributions of (a) the contact pressure and (b) slip

vector norm under pyramidal-indenter at the maximum indentation depth

of $7 \overset{o}{A}$. (stress unit : GPa; length unit: Angstrom)
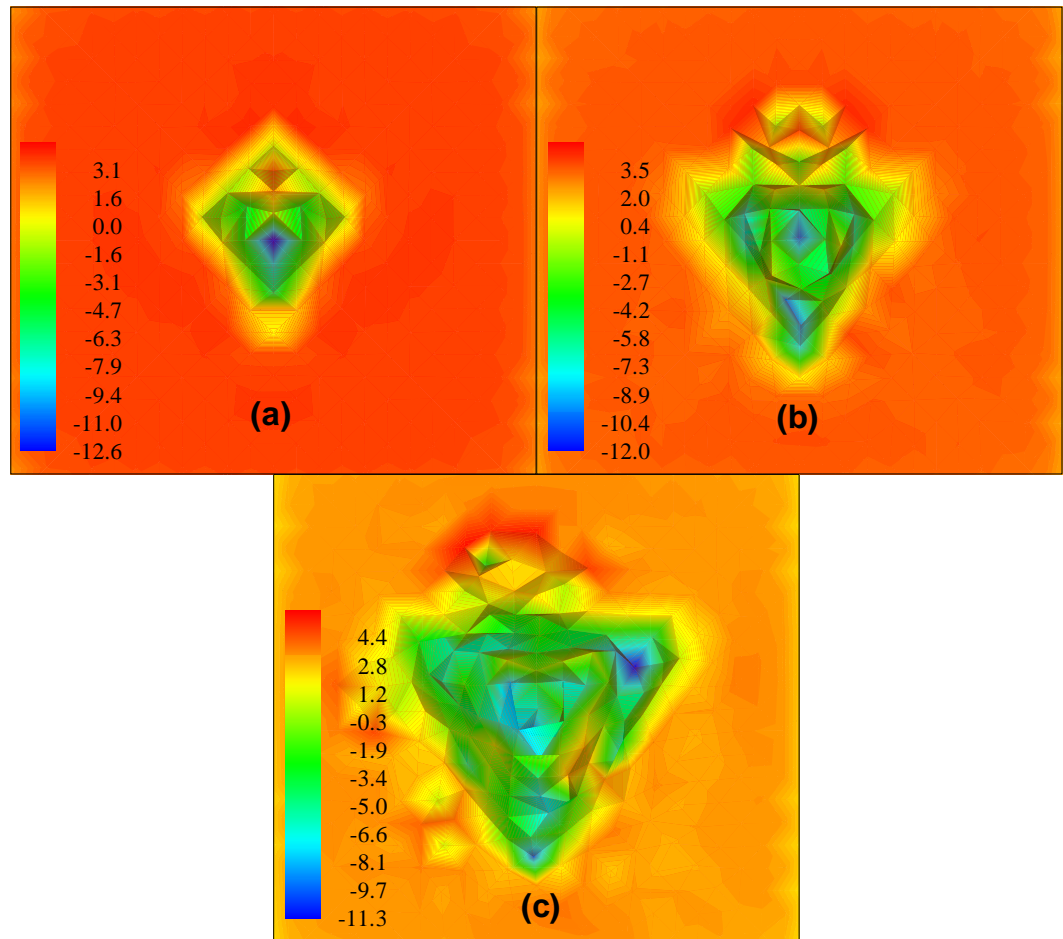
Figure 3 Top views of the distributions of the contact pressure under pyramidal-indenter at the maximum indentation depth of (a) $4\overset{o}{A}$, (b) $7\overset{o}{A}$, and (c) $10\overset{o}{A}$. (stress unit: GPa)
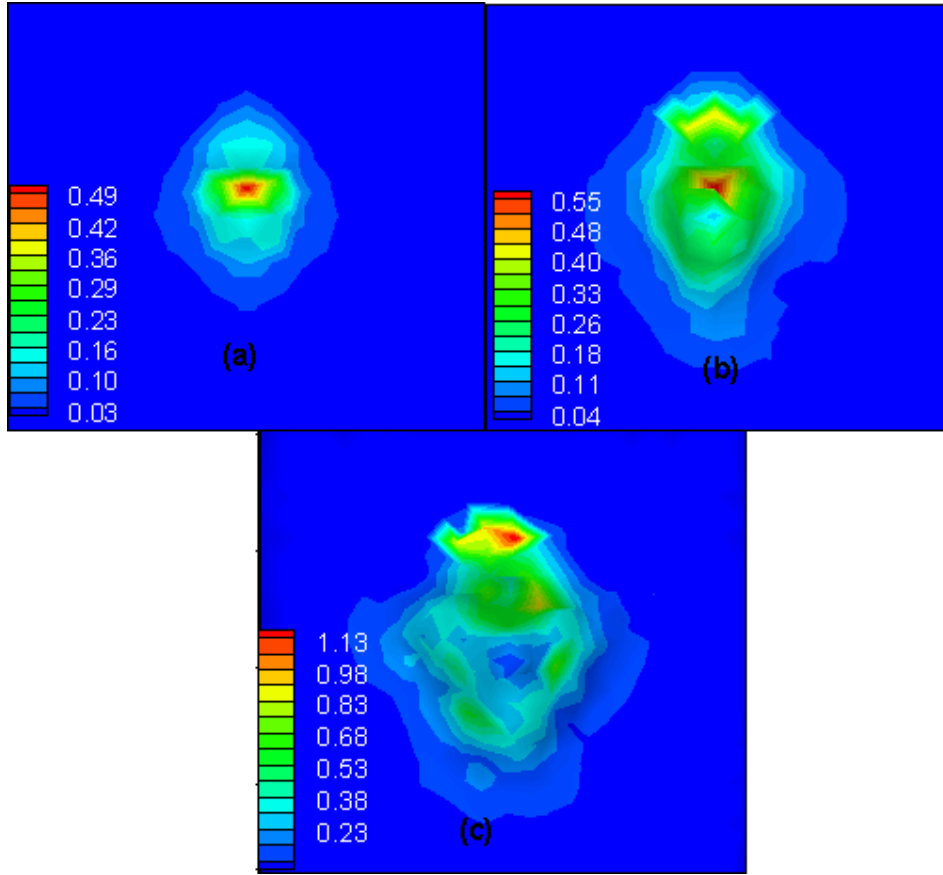
Figure 4 The subplots of the distributions of the strain gradient viewed from [001]

direction for indentation depth: (a) $4\overset{o}{A}$ (b) $7\overset{o}{A}$ (c) $10\overset{o}{A}$. (Strain gradient

unit : $1/\overset{o}{A}$)
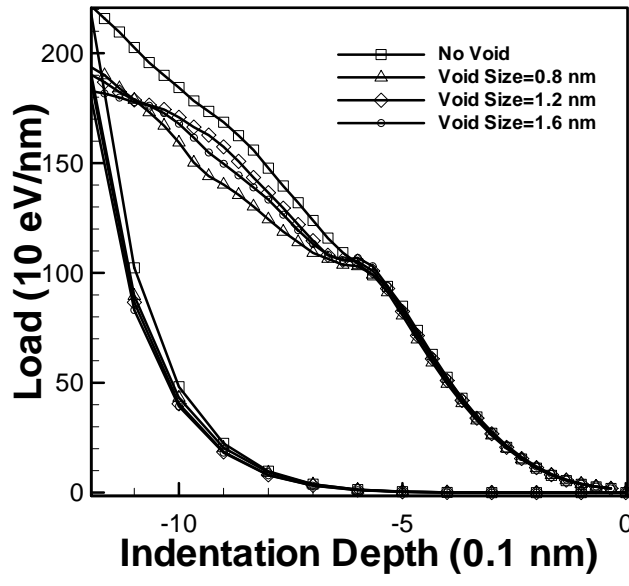
(a)variation of void size
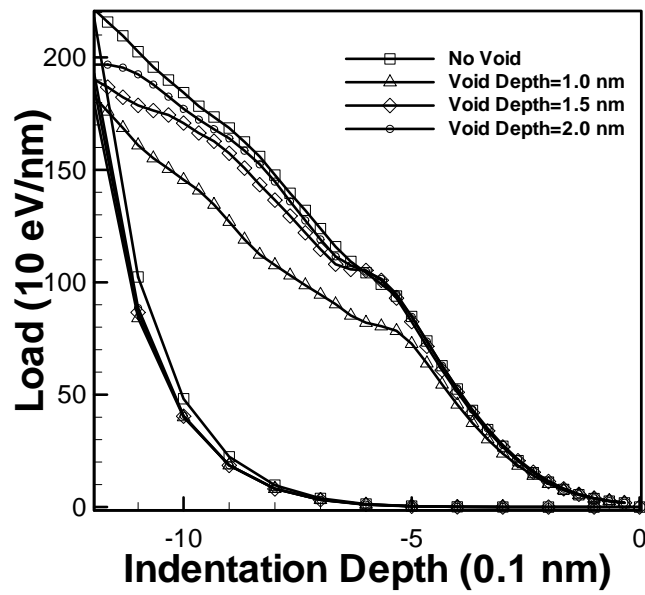
(b)variation of void depth

Figure 5 Load-depth curves for two void parameters: (a) void size, and (b) void depth.
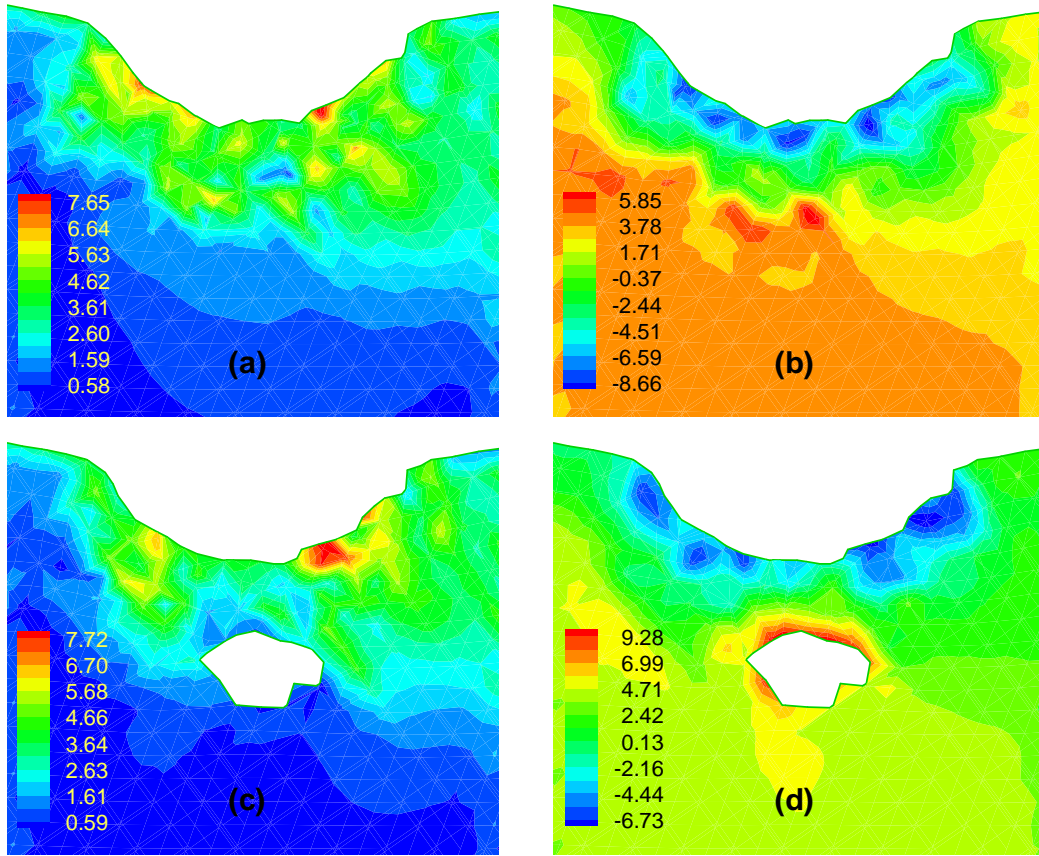
Figure 6. Distributions of hydrostatic stress and von Mises stress in cross-section through indenter and parallel with (-1 01) plane: (a) von Mises stress for no void. (b) hydrostatic stress for no void. (c) von Mises stress for void size=1.2 nm and depth=1.5 nm. (d) hydrostatic stress for void size=1.2 nm and depth=1.5 nm. (Stress unit: GPa)
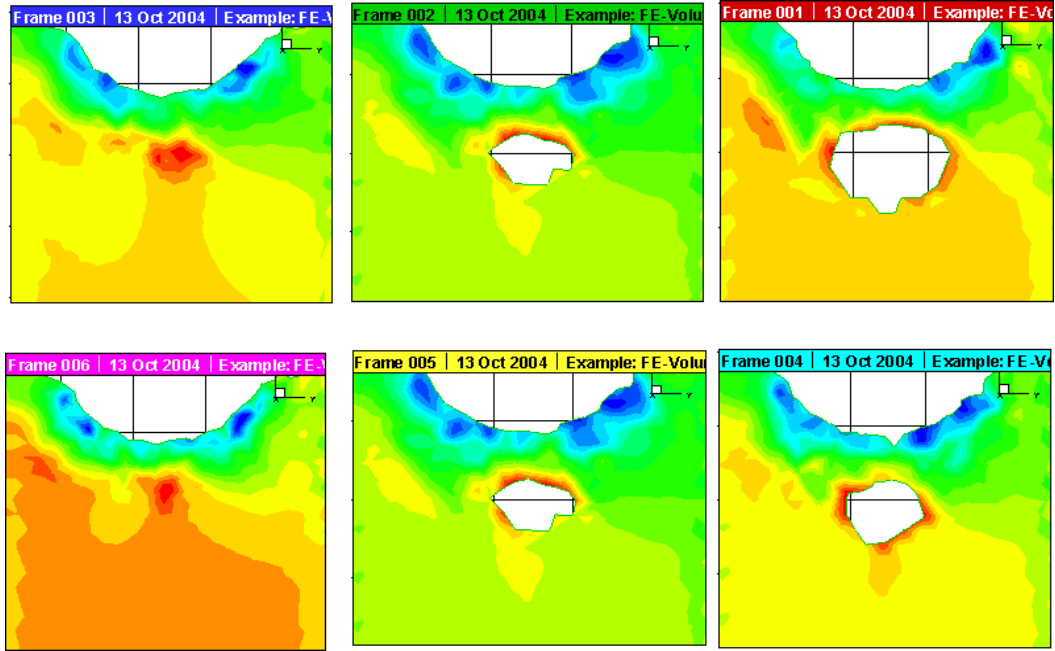
Figure 7 Variation of hydrostatic stress distribution in cross-section through indenter tip with two void parameters: (a)~(c) void size=0.8, 1.2, and 1.5 nm. (d)~(f) void depth=1.0, 1.5, and 2.0 nm.
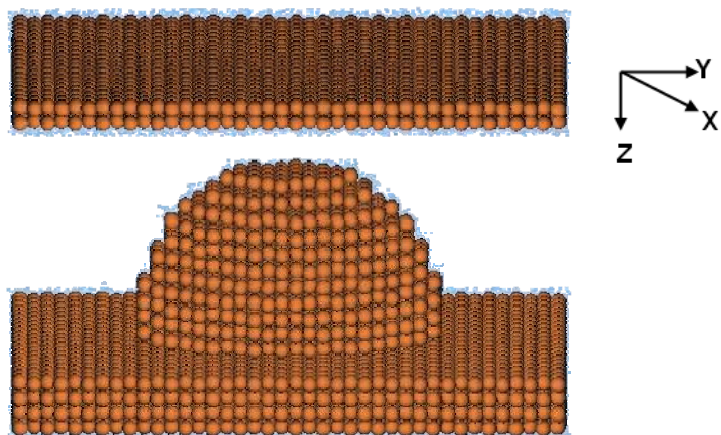
Figure 8   Simulation model comprising rigid carbon upper plate and annealed

asperity on copper substrate.
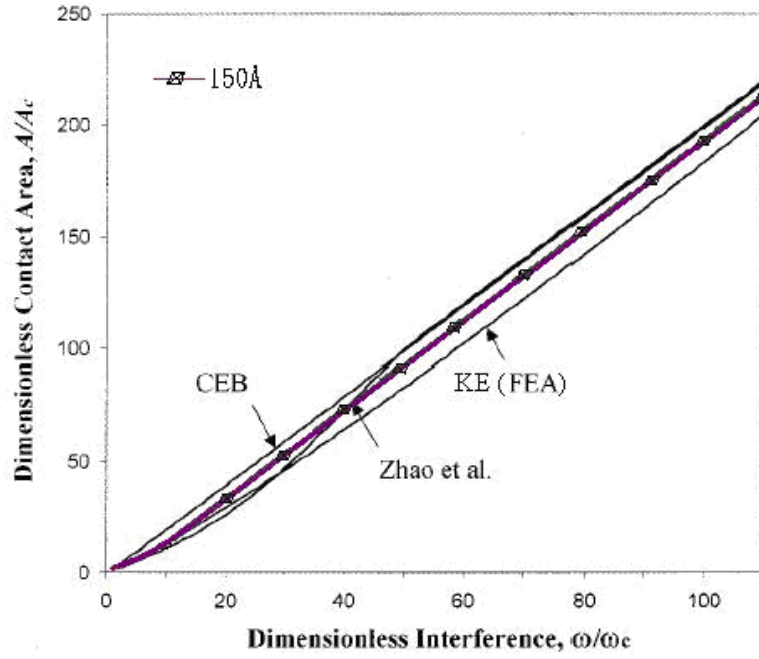
(a)
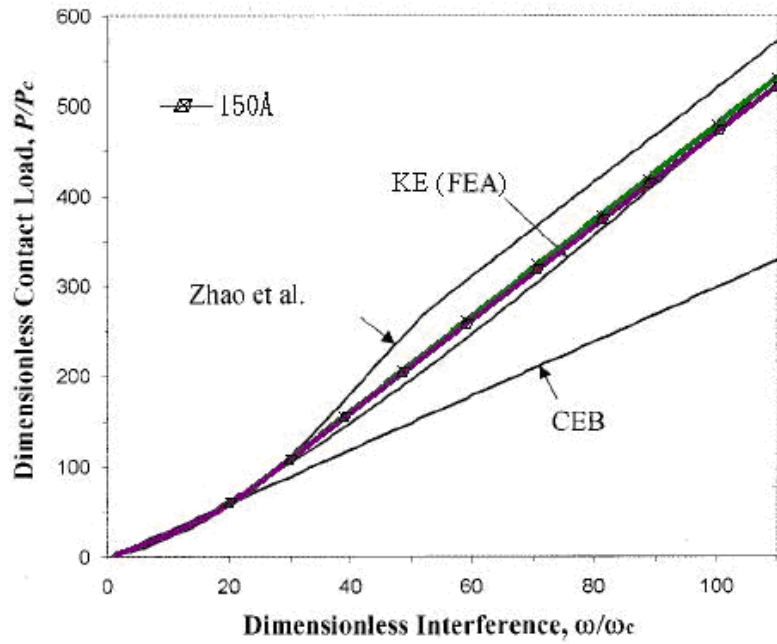
(b)

Figure 9 (a) Variation of dimensionless contact area (A/A$_c$) with dimensionless interference (ω/ω_c); and (b) variation of dimensionless contact load (P/P$_c$) with dimensionless interference (ω/ω_c).

47
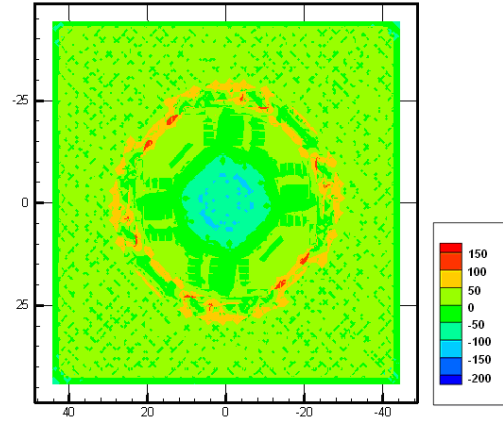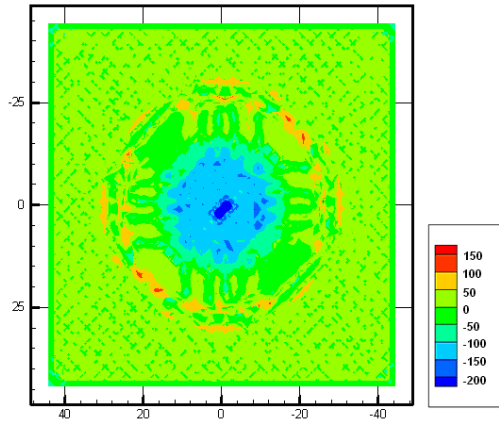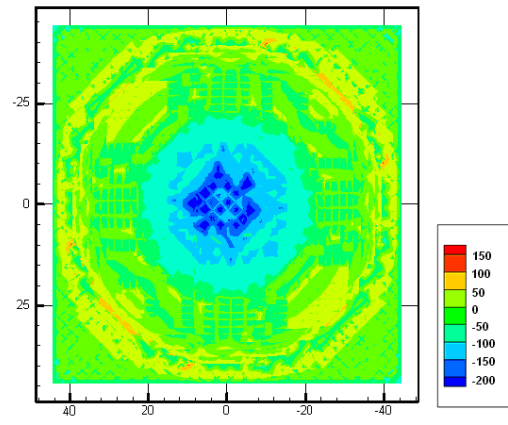
Figure 10 Plane views of contact load distribution under various displacement
of (a) *8* Å, (b) 16 Å and (c) 24 Å.
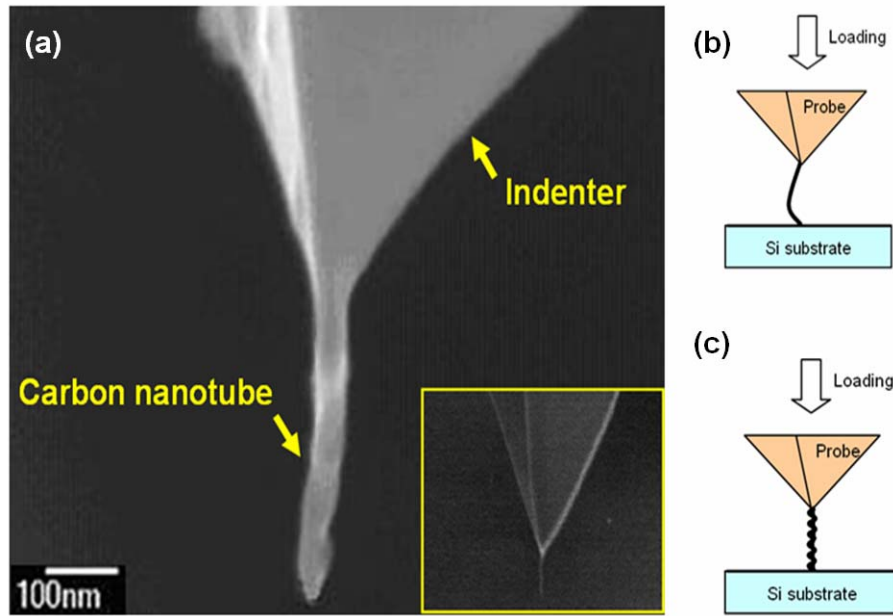
Figure 11 (a) Transmission electron microscopy (TEM) image of carbon nanotube probe, and Scanning electron microscope (SEM) image of carbon nanotube probe, (b) schematic illustration of local-buckling in nanotube probe, (c) schematic illustration of global-buckling in nanotube probe.
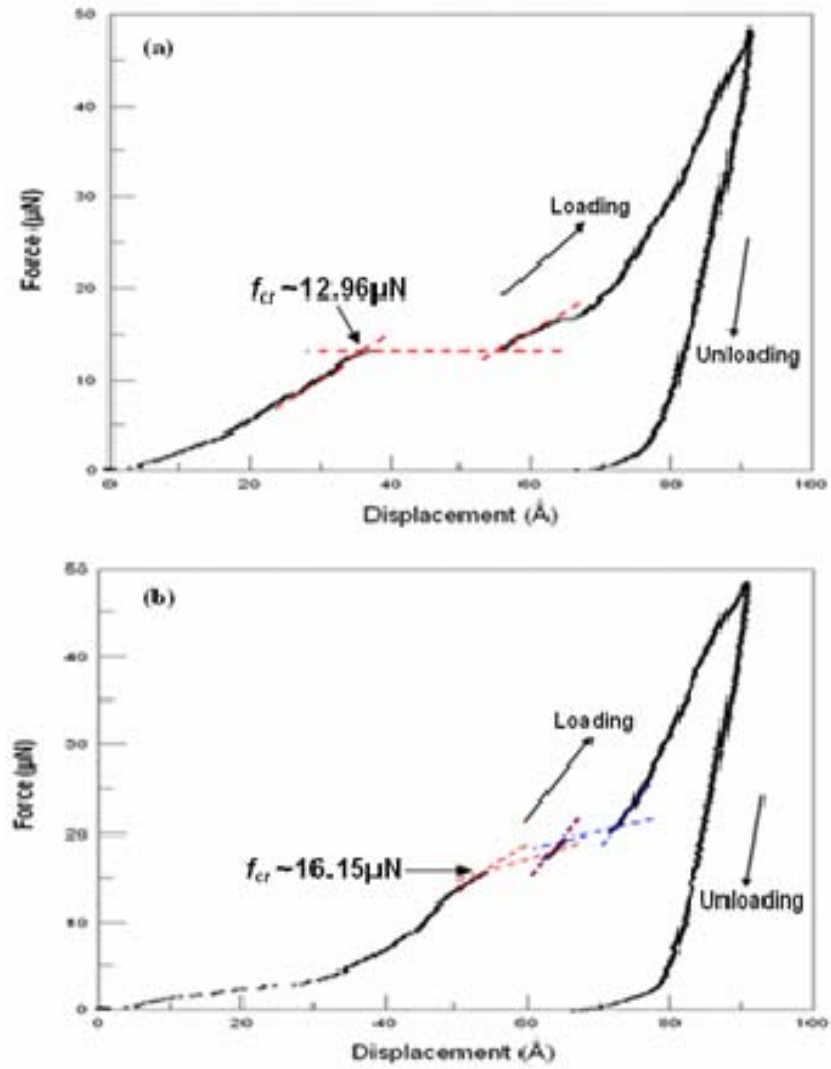
Figure 12.   Representative force-displacemen curves during experimental

nanoindentation: (a) 300nm sample, and (b) 100nm sample,

respectively.
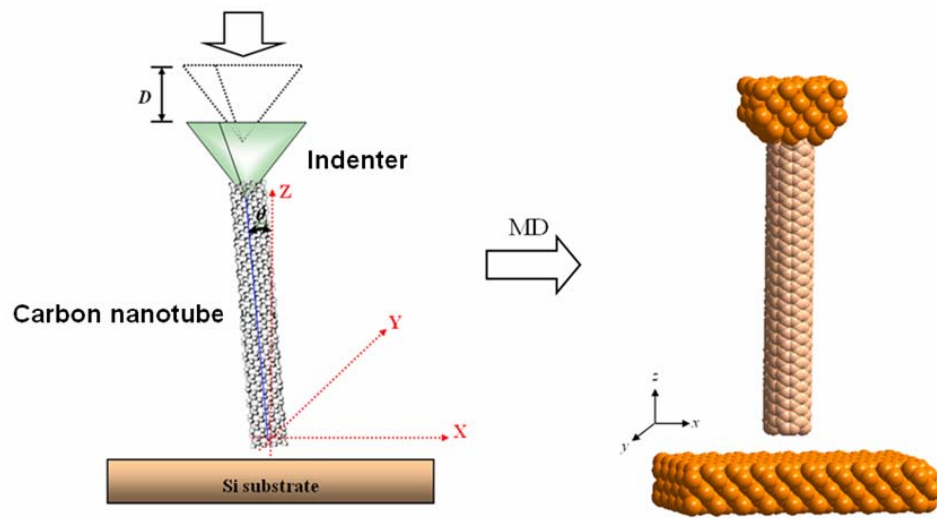
Figure 13. Schematic representation of MD simulation model. [*D* denotes downward displacement of indenter and *θ* indicates initial inclination angle.]
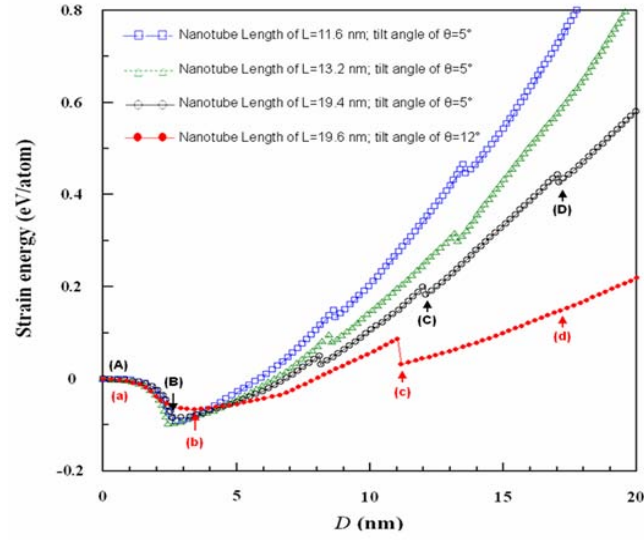
(a)
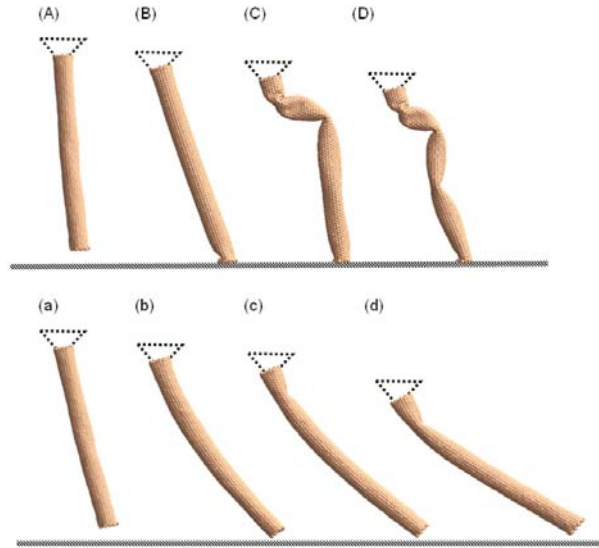
(b)

Figure 14. (a) Variation of strain energy with downward displacement of indenter for carbon nanotube probes with various lengths and inclination angles, and (b) Snapshots of buckling instability in nanotube probes during nanoindentation. [Labels (A)–(D) and (a)–(d) denote different stages of global-buckling and local-buckling, respectively. Note that these labels correspond to the labels presented in Figure 14(a).]
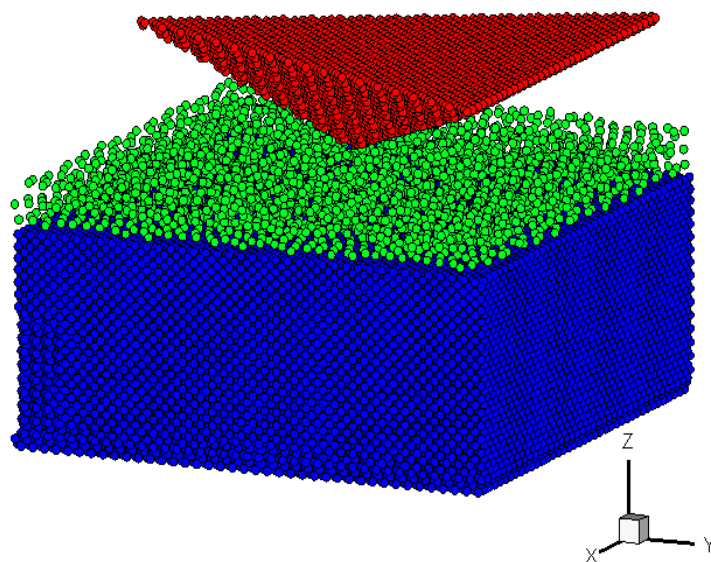
Figure 15. Initial simulation model for nanoindentation process showing Cu monocrystal slab, diamond indenter and polymer adsorbed layer.
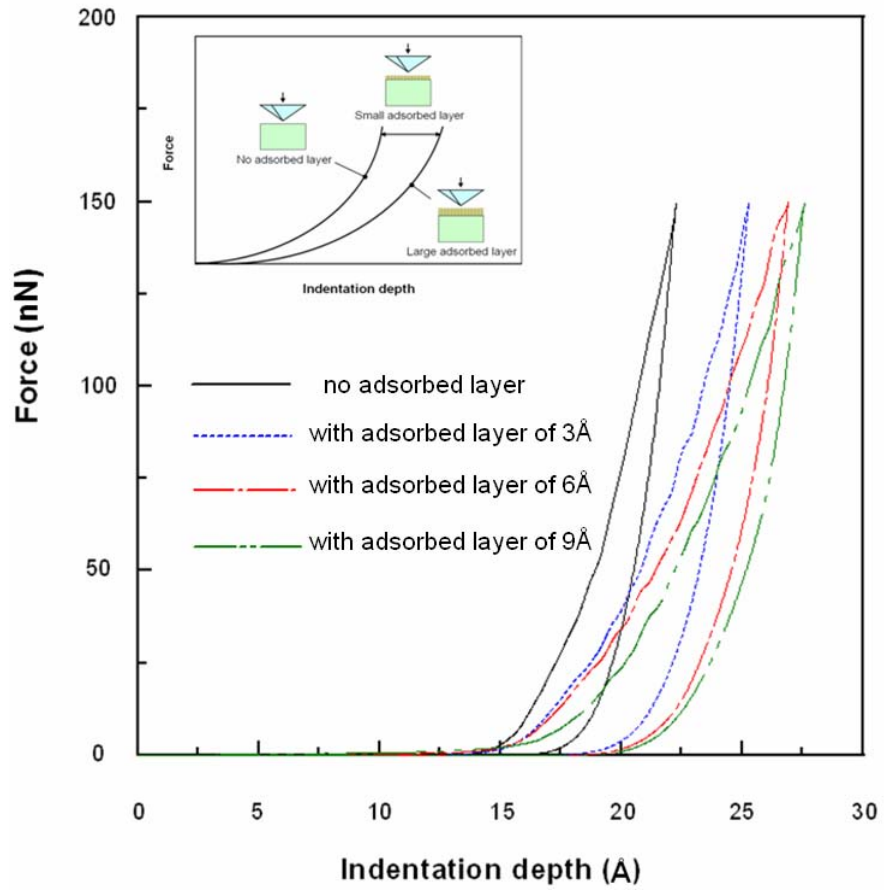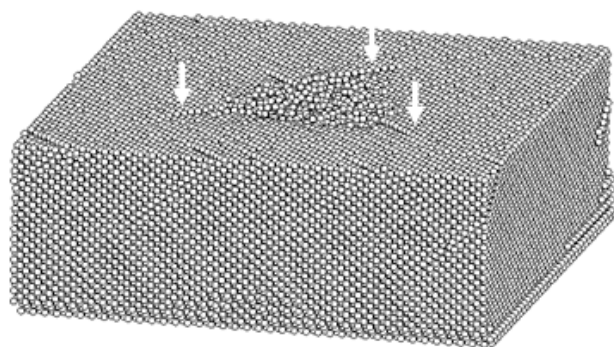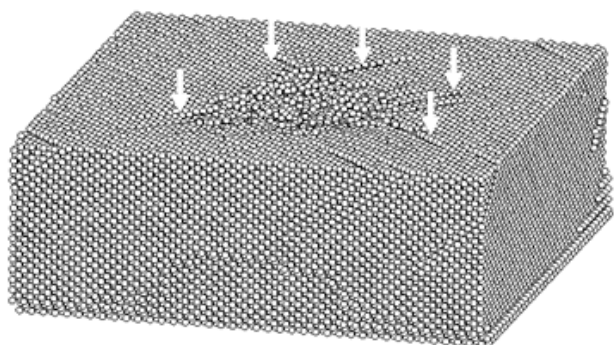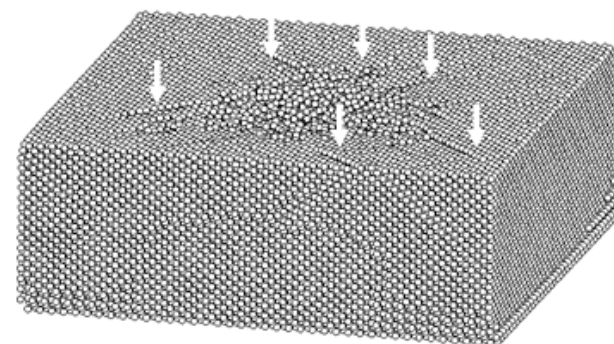
Figure 16. Representative load-displacement curves for nanoindentation of single-crystal Cu substrate with no adsorbed layer and with adsorbed layer of thickness 3, 6, 9Å, respectively.

Figure 17. Atomic configuration of Cu substrate with adsorbed layers of thickness: (a) 3Å, (b) 6Å and (c) 9Å during unloading stage. Note the presence of slip planes indicated by red arrows.